Science
AAAS

Supplementary Materials for

Imaging the breaking of electrostatic dams in graphene for ballistic and viscous fluids

Zachary J. Krebs *et al*.

Corresponding author: Victor W. Brar, vbrar@wisc.edu

Science **379**, 671 (2023)
DOI: 10.1126/science.abm6073

The PDF file includes:

Materials and Methods

All measurements were performed in a commercial, low-temperature STM (CreaTec GmbH, Germany). The sample was fabricated by mechanically exfoliating graphene flakes (Graphene Supermarket) on Si^{++} wafers with 285 nm of SiO_2. Graphene flakes were viscoelastically stamped with 80 nm-thick exfoliated hBN following standard procedures (*81*,*82*). After constructing the stack, it was inverted and annealed in high vacuum at 300°C. The graphene was grounded using electron beam lithography by depositing two Cr/Au electrodes (layer thickness of 3 nm and 150 nm, respectively) on each end of the flake. In order to ensure a pristine surface, the sample was annealed in an Ar/H_2 (100/10 sccm) environment at 400°C for 40 min at a total pressure of 476 mbar before being transferred into a UHV environment for further annealing at 250°C and 10^{-10} mbar for at least 12 hours. The sample was then transferred – without breaking vacuum – into the cryostat, with base pressure $< 8 \times 10^{-11}$ mbar.

The dimensions of the graphene flake are 30 μm lengthwise along the direction of current flow and 15 μm wide. The measurements presented in the main text were replicated two separate times at 4.5 K and two times at 77 K, each with different STM tips and electrostatic barriers. Electrochemically etched PtIr STM tips were used for each of these experiments, except for the 77 K data in the main text which was recorded using a W tip. Source-drain current was supplied by a Yokogawa GS200 DC Voltage/Current Source.

Supplementary Text

Transport properties of the graphene device

We characterized the macroscopic transport properties of our graphene/hBN device by recording the current and resistance as a function of back gate voltage while applying a fixed source-drain voltage. In Fig. S1A, we plot the total current against V_g at both low and high temperature with source-drain bias $V_{sd} = 400$ mV. At 77 K, the current is slightly less than the data at 4.5 K, by about 10-20 μA, over all gate voltages. This confirms that our sample quality and doping did not significantly change between measurements. To check the linear response of the total current, we recorded the same data at 4.5 K except with the source-drain bias reduced by a factor of 8 ($V_{sd} = 50$ mV). By multiplying the measured current by 8, we obtain good agreement between the low and high V_{sd} data, suggesting that we are operating in a macroscopic linear response regime even at a 'high' source-drain bias of 400 mV. We note that the quoted source-drain bias is applied across the graphene sample and a 1 kΩ, 1 kHz low-pass filter in series, so the actual voltage difference between the graphene leads is ~ 25 mV and 200 mV for $V_{sd} = 50$ mV and 400 mV, respectively. In Fig. S1B, we present the device resistance versus V_g at both electron and hole doping. There is a single resistance peak near $V_g = 0$, the location of the charge neutrality point (CNP) for all measurements presented in the text.

Prior to creating electrostatic barriers on our samples, we first obtained spatial maps of the electrochemical potential μ_{ec} while driving $I_{sd} = 190$ μA through the bare graphene/hBN sample at a low carrier density ($n = -1.4 \times 10^{11}$ cm^{-2}), as shown in Fig. S2 along with a simultaneously acquired topographic image. These data reveal a potential drop of 420 μV/μm, which corresponds to a mean free path of $l_{mr} = 5$ μm obtained via the Drude conductivity $\sigma = e^2 v_F l_{mr} D(E_F)/2$, where v_F is the Fermi velocity and $D(E_F)$ the density of states at the Fermi level (*83*). Some local deviations in μ_{ec} are also seen on top of the linear background in Fig. S2B, which we attribute to scattering near charged defects buried in the hBN substrate.

Electrochemical potential along transverse linecuts

In the main text we plot the electrochemical potential along linecuts through the channel in the direction of current flow. In Fig. S3 we also address the transverse direction – that is, along a line connecting the centers of the two potential wells defining the channel. Far away from the p-n junction boundaries (> 50 nm), the electrochemical profiles are relatively flat. Near the p-n junction boundaries, however, the electrochemical potential is extremized. We suspect that strong resonances in the graphene local density of states induced by tip gating leads to appreciable thermovoltages within ~50 nm of the p-n boundary, and for this reason we do not interpret these extrema as being due to novel transport or hydrodynamic effects. Instead, we use the distance between electrochemical extrema to determine the channel width w at each gate voltage that is used in our calculations of the conductance G_{data}. Additionally, the electrochemical potentials used in our calculation of $\Delta\mu_{ec}$ are recorded at distances greater than 50 nm away from the p-n boundaries to avoid an extra thermovoltage contribution; nevertheless, a nonzero thermovoltage contribution would be subtracted out anyways since only electrochemical differences are needed to calculate the conductance. In Fig. 2 of the main text, the CNP rings defining the p-n junctions appear bright at 4.5 K (maxima in Fig. S3A) and dark at 77 K (minima in Fig. S3B) under transport using V_{sd} = 400 mV. In Fig. S3C, we include extra data showing an inversion of the ring (bright-to-dark) at 4.5 K when the source-drain bias is lowered to 20 mV. These results show that the appearance of the ring is dependent on the magnitude of the source-drain bias and current running through the sample, which points to a thermal effect.

Linear response regime for current flow through channels

We present the conductivity at a lower source-drain bias, V_{sd} = 50 mV (smaller by a factor of 8 than is used for the results of the main text), in Fig. S3. We find that the conductivities obtained at both source-drain voltages are nearly the same. This suggests that the key findings in the main text are robust down to smaller source-drain voltages, and that electronic heating caused by the higher source-drain current does not impact the measured electrochemical potential drops. For channel widths larger than 400 nm, the extracted conductivity grows larger than the Sharvin prediction. For this reason we limit our analyses to channel widths less than 400 nm where the Sharvin formula is valid.

Repeated measurements

A repeated measurement of the channel conductivities using different electrostatic dams in a different area of the graphene flake reproduces the key findings in the main text (Fig. S5A): the channel conductances at 4.5 K agree very well with the Sharvin formula assuming $\alpha = 2.8$, while the conductivities at 77 K are enhanced beyond the Sharvin prediction and can be fit by adding a viscous contribution using the same value of the e-e scattering length, l_{ee} = 300 nm. In Fig. S5B, we show that the 77 K conductance data presented in the main text cannot be fit even by adjusting the proportionality factor α, which necessitates the addition of a viscous contribution to the conductance G_G.

Calculation of the Landauer residual resistivity dipole (LRRD) profile as a function of l_{ee} and barrier radius, r

We derive the resistivity dipole potential from Ref. 70, which is plotted in Fig. 3C and D of main text. One can deduce that the electric field is given by

$$\vec{E}(\vec{k}) = -i\vec{k}\frac{2jU(\nu)}{ie^2v_F^2N}\frac{\cos\theta_k}{k} \tag{S 1}$$

where j is the applied current density, N is the density of states, v_F is the Fermi velocity, $\theta_k = \hat{k}\cdot\hat{x}$ (without loss of generality, the external current is applied in the x direction), and U(ν) is the scattering strength renormalized by viscosity ν. It has been shown that U(ν) is given by

$$U(\nu) = \frac{U_0}{1+\frac{U_0}{4\pi\nu}\ln(L/\overline{a})}, \qquad \overline{a} = \sqrt{eal_{ee}/2} \tag{S 2}$$

here a is the scatterer radius and L is the distance between scatterers. Since $\vec{E} = -\nabla V$, the potential is written as

$$V(\vec{k}) = \frac{2jU(\nu)}{ie^2v_F^2N}\frac{\cos\theta_k}{k} \tag{S 3}$$

Taking a Fourier transform back to the real space, $V(\vec{r}) = \int_0^\infty \frac{kdk}{2\pi}\int_0^{2\pi}\frac{d\theta_{kr}}{2\pi}e^{i\vec{k}\cdot\vec{r}}V(\vec{k})$ where $\theta_{kr} = \hat{k}\cdot\hat{r}$, one has

$$V(\vec{r}) = \frac{jU(\nu)}{i\pi e^2v_F^2N}\frac{1}{r}\int_0^\infty d\tilde{k}\int_0^{2\pi}\frac{d\theta_{kr}}{2\pi}e^{i\tilde{k}\cos\theta_{kr}}\cos\theta_k,\ \tilde{k} = kr \tag{S 4}$$

Using the identity

$$\cos\theta_k = \cos\theta_{kr}\cos\theta - \sin\theta_{kr}\sin\theta, \qquad \theta = \hat{r}\cdot\hat{x} \tag{S 5}$$

the angular integration gives

$$\int_0^{2\pi}\frac{d\theta_{kr}}{2\pi}e^{i\tilde{k}\cos\theta_{kr}}\cos\theta_k = i\cos\theta\,J_1(\tilde{k}) \tag{S 6}$$

and the integration over $\tilde{k}$ is straightforward. As a consequence, we obtain the dipole potential (in two dimensions)

$$V(\vec{r}) = \frac{p\cos\theta}{r} \tag{S 7}$$

where the dipole moment p is given by

$$p = \frac{jU(\nu)}{\pi Ne^2v_F^2} = \frac{j}{2\pi\sigma n_s}\frac{U(\nu)}{U_0} \tag{S 8}$$

Here n_s is the number density of the scatterers and $\sigma = Ne^2 v_F^2 / (2n_s U_0)$ is the Drude conductivity. In the ballistic limit, $U(\nu) \approx U_0$, and $p \approx j / (\sigma n_s)$. In the hydrodynamic limit, U(ν) drops to U(ν) ≈ 4πν, hence the dipole moment is

$$p \approx \frac{2j}{\sigma n_s}\frac{\nu}{U_0} \tag{S 9}$$

Nonlinear screening

It is noteworthy that in our numerical simulations we have adopted hard wall potentials at the boundaries of the two circular barriers and neglected the nonlinear screening effects of the p-n interface. Accounting for these effects requires self-consistently solving the Poisson equation coupled with hydrodynamic flow equations 5 and 6 (in main text). However, a reasonable estimate of the effects of nonlinear screening can be found by analytically calculating the static screening around a single circular p-n junction without considering hydrodynamic flow. Using this method (described below), we estimate a nonlinear screening length of <100 nm for a stepwise p-n junction, indicating that the macroscopic electron flow description gives a reasonably accurate approximation everywhere except for in close proximity to the junction.

With regards to how the long screening length may affect our results, we first note that the screening length of the p-n junction sets the distance at which the junction is totally screened. While the electron can begin to scatter off the p-n junction as it becomes unscreened, there is no hard wall set by the screening length, and most scattering would still occur at the classical turning point of the p-n barrier. We also note that the screening length is calculated for a discontinuous boundary, that sharply steps up at a given position. In our actual experiment, the potential barrier is smoothly varying, and more efficiently screened. In both cases (finite screening or curved potential), there is a correction of flow only within the screening length of the junction, but does not modify the flow outside of the screening length which is the emphasis of the simulations shown in Fig. 6 of the main text.

We provide self-consistent solutions to the electric potential and charge density for a single circular p-n junction without considering the hydrodynamic flow. To facilitate our discussion, we denote the background charge density created by external gates as $\rho_b(r)$, which can be approximated as $\rho_b(r) = \rho_b' r$ for the entire p-n junction width (the p-n interface is shifted to the origin r = 0). The electric potential and the density can be solved from the following coupled equations

$$\begin{aligned} &\frac{\kappa}{e}V(r) = \int_0^\infty \frac{4r'dr'}{r+r'}K\left(\frac{2\sqrt{rr'}}{r+r'}\right)\left[\rho_b(r') - \rho(r')\right], \\ &\mu[\rho(r)] - eV(r) = 0, \qquad \mu(\rho) = \sqrt{\pi}\hbar v_F\sqrt{|\rho|}, \end{aligned} \tag{S 10}$$

where κ is the dielectric constant and *K(k)* is the elliptic integral of the first kind with modulus *k*. In Eq. S10, we assumed the Thomas-Fermi (TF) approximation. It is then evident that within the TF approximation, the charge density satisfies the following equation:

$$\sqrt{\rho(r)} = \frac{\alpha}{\sqrt{\pi}} \int_0^{\infty} \frac{4r'dr'}{r+r'} K\left(\frac{2\sqrt{rr'}}{r+r'}\right)\left[\rho_b' r' - \rho(r')\right]. \qquad \text{(S 11)}$$

The solution to Eq. S11 gives the universal spatial profile of the charge density/potential, but it requires numerical evaluation. Nevertheless, one is still able to draw several qualitative conclusions from Eq. S11. Following similar analysis of a planar junction in Ref. 84, it can be shown that for small interaction constant $\alpha < 1$, in the region $|r| \gg l_s \sim \left(\alpha^2 \rho_b'\right)^{-1/3}$, one has almost perfect screening, which can be described by TF approximation; in the region $l_{TF} \sim \sqrt{\alpha} l_s \ll |r| \ll l_s$, the screening effect is poor but the TF approximation still holds; in the immediate vicinity of p-n interface, $0 < |r| < l_{TF}$, the TF approximation breaks down and one needs to compute the electron wavefunction in order to obtain the potential and the charge density (*84*). Given the material parameters, we have $\alpha \approx 0.8$, $l_s \sim 116$ nm, $l_{TF} \sim 103$ nm. The various domains and length scales are summarized in Fig. S5. This means that almost everywhere except for a close proximity to the interface the macroscopic electron flow description gives reasonably accurate approximation. We next provide numeric solution to Eq. S2 by collocation methods with Bernoulli wavelets. To this end, let us rescale all length scales by D, the junction width, charge density by $1/D^2$ and electric potential by $\sqrt{\pi}\hbar v_F / eD$, then Eq. S11 transforms to the following dimensionless form,

$$V(x) = \frac{4\alpha \Delta\rho D^2}{\sqrt{\pi}} \int_0^1 dy \frac{y^2}{x+y} K\left(\frac{2\sqrt{xy}}{x+y}\right) - \frac{4\alpha}{\sqrt{\pi}} \int_0^1 dy \frac{y}{x+y} K\left(\frac{2\sqrt{xy}}{x+y}\right) V^2(y) \qquad \text{(S 12)}$$

where $\Delta\rho$ is the density difference across the p-n junction, and $\Delta\rho D^2 \approx 10^3$. The profile of $V(r)$ and $\rho(r)$ in the range of $0 < r < D$ are shown in Fig. S6.

Ohmic and viscous fluid simulations

The current flow in the both the Ohmic and viscous regimes are simulated by numerically solving Eq. 6 of the main text in Mathematica, using the "NDSolveValue" function with no-slip boundary conditions for the barriers and graphene flake edges.

Perfect slit geometry and estimation of c_G

To estimate the value the non-universal constant c_G that goes into the Gurzhi conductance, Eqs. 2 and 3 in the main text, we first simulate the viscous flow of current through a perfect slit geometry where the value of c_G is already known analytically ($\pi^2/16$), see Fig. S7. We then compare the simulated potential drop and current through the slit with the results from the circular barrier simulation (Fig. 5). We find that in the circular barrier simulation, the conductance is 1.22 times larger, which means the correct non-universal constant to use is $c_G = 1.22 \times \pi^2/16 = 0.75$.

Comparing channel currents in ballistic and viscous transport regimes

The current flowing through the channel $I_{channel}$ – determined by the parameter □ – in the ballistic and viscous regimes were estimated using different methods. In the ballistic case, □ was determined to be 2.8 by fitting the channel width dependence of the conductance at 4.5 K using the Sharvin formula (Eq. 1 in the main text). This fitting is premised on the ballistic nature of the electrons, which we established by measuring the momentum-relaxing scattering length of the electrons to be around 5 μm, and by using the results of other experimental works that measured the momentum-relaxing scattering lengths to be >20 μm at cryogenic temperatures *(38)*. In the viscous case, we estimate the channel current by numerically solving the hydrodynamic equation (Eq. 6 in the main text) assuming a Gurzhi length of l_G = 0.6 μm, which was found by plugging the experimentally determined quantities l_{ee} = 300 nm and l_{mr} = 5 μm into $l_G = \sqrt{l_{ee} l_{mr}}/\,2$. In Fig. S8 we plot the channel current density normalized by the average current density across the graphene flake, $j_{current} / j_{average}$, for a range of Gurzhi lengths, and indicate the result for l_G = 0.6 μm relevant to our experimental conditions at T = 77 K. This represents a self-consistent approach: l_{ee} is first calculated by fitting the experimental data for a given □, which is then used to compute l_G for the hydrodynamic simulations to show that the same current flows through the channel. This method yields □ ~ 3, in good agreement with the ballistic case of □ ~ 2.8. We note, however, that our simulations with hard boundaries do not use the exact same potential profile as the experiment, where there is a smoothly varying potential. For this reason, we use □ ~ 2.8 for both cases in the manuscript. Using □ ~ 3 would lead to minor changes in our analysis that would lie within the tolerance set by unknowns in the boundary conditions of fluid flow.

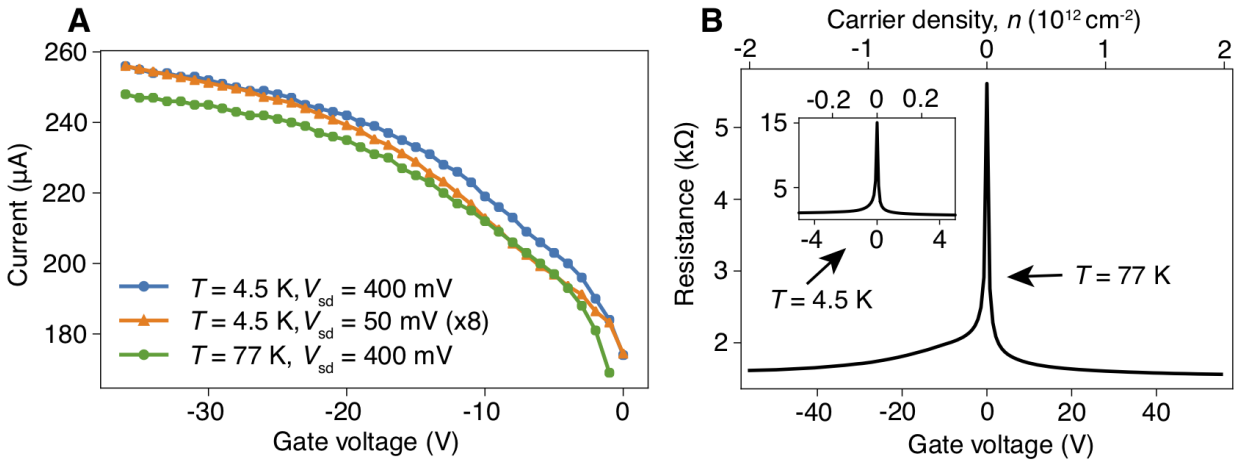

Fig. S1. Transport characteristics of our graphene/hBN device. (A) Current measured across the device as a function of gate voltage at high and low temperature and source-drain voltage (after the creation of electrostatic barriers). **(B)** Device resistance as a function of gate voltage and carrier density at 77 K (before the creation of electrostatic barriers). Inset: resistance at 4.5 K, zoomed-in near the CNP.

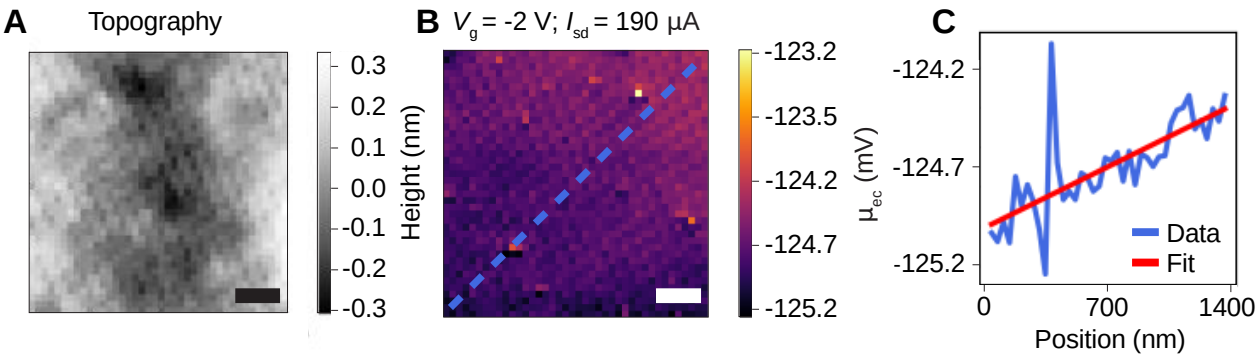

Fig. S2. Measuring the conductivity of clean graphene with STP. (A) Topographic STM image of a 1 x 1 µm area of graphene on hBN. Scale bars are 200 nm. **(B)** Simultaneously acquired STP image from the same area obtained with I_{sd} = 190 µA (V_{sd} = -0.4 V) across a 30 µm long sample that has an average width of 15 µm. The periodic texture observed in both images is an aliasing effect created by the graphene/hBN Moiré potential and the measurement grid. **(C)** Measured electrochemical potential along the flow direction and dashed line indicated in (B). The best fit line is shown in red (slope = 420 ± 10 µV/µm).

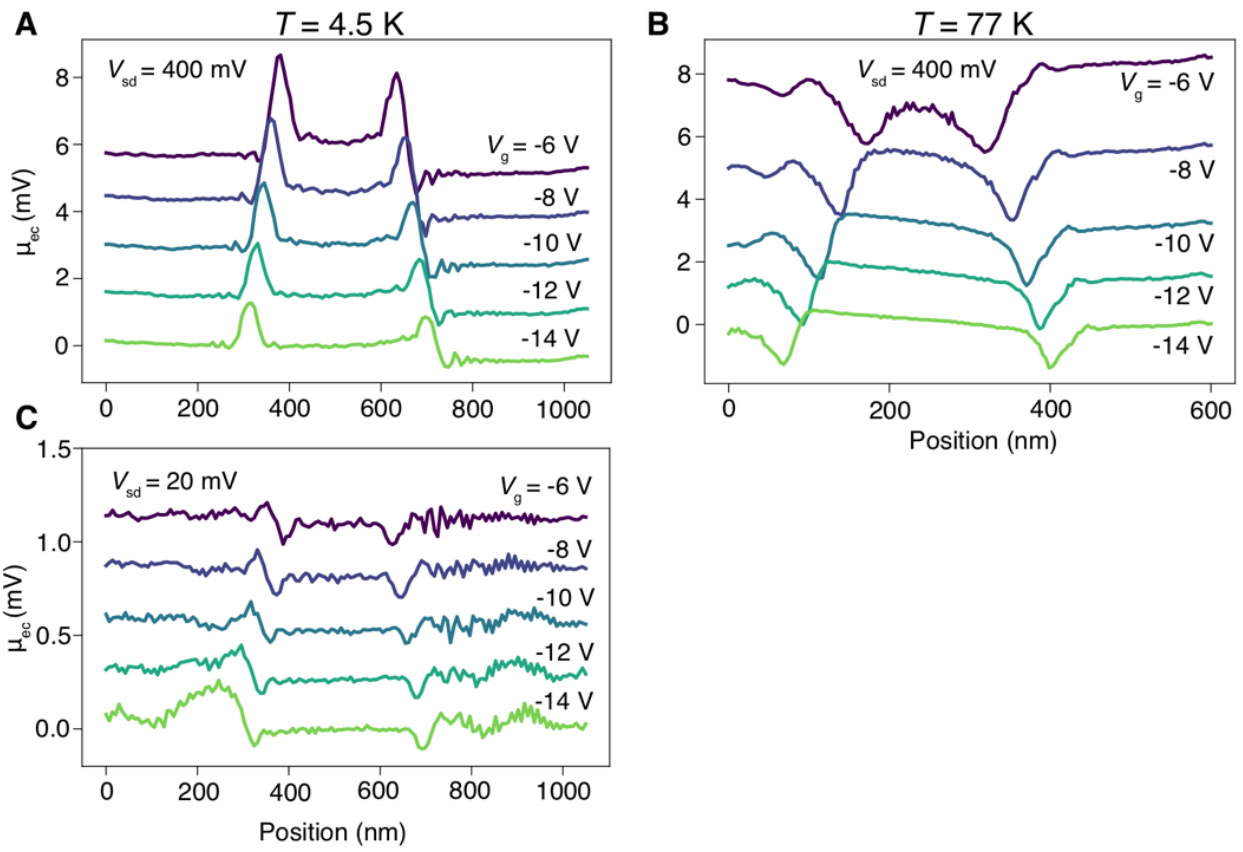

Fig. S3. Tracking the electrochemical potential along transverse linecuts through the channel. (A) Electrochemical potential profile along a transverse linecut across the channel at low temperature (4.5 K) and varying channel widths. **(B)** Transverse electrochemical potential linecuts within the channel at high temperature (77 K). **(C)** Same as (A), but with a much smaller source-drain bias, 20 mV. The peaks at the boundaries of the p-n junctions are now inverted with respect to those in (A).

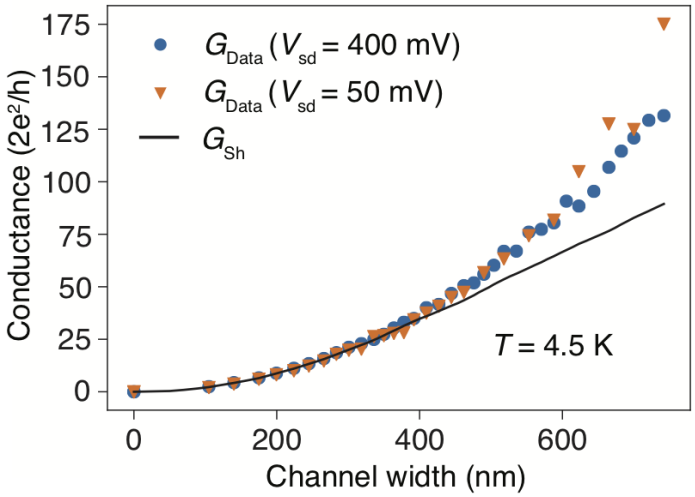

Fig. S4. Calculated channel conductance $G_{data} = I_{channel} / \Delta\mu_{ec}$ obtained by using both a high (400 mV) and low (50 mV) source-drain bias.

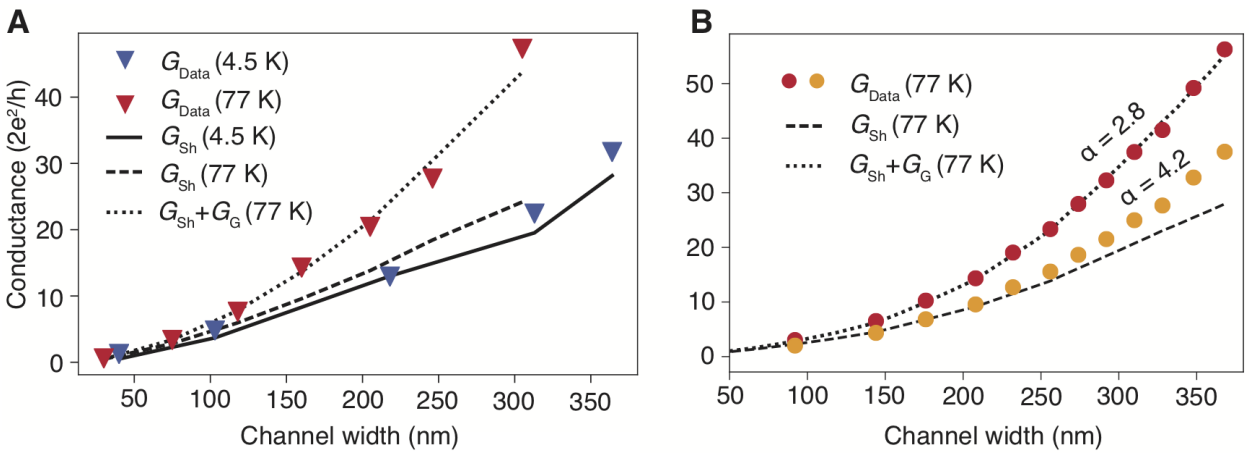

Fig. S5. Channel conductivities from a repeated measurement, and attempts to fit the 77 K data without a viscous contribution. (A) Channel conductance $G_{data} = I_{channel} / \Delta\mu_{ec}$ derived from a repeated measurement using different p-n junction barriers. The theoretical curves are good fits assuming $\alpha = 2.8$ and $l_{ee} = 300$ nm, the same values used in the main text. **(B)** Attempts to fit the 77 K conductance data in the main text to the Sharvin formula without including a viscous contribution by increasing α to 4.2 (yellow points), leading to a poor fit.

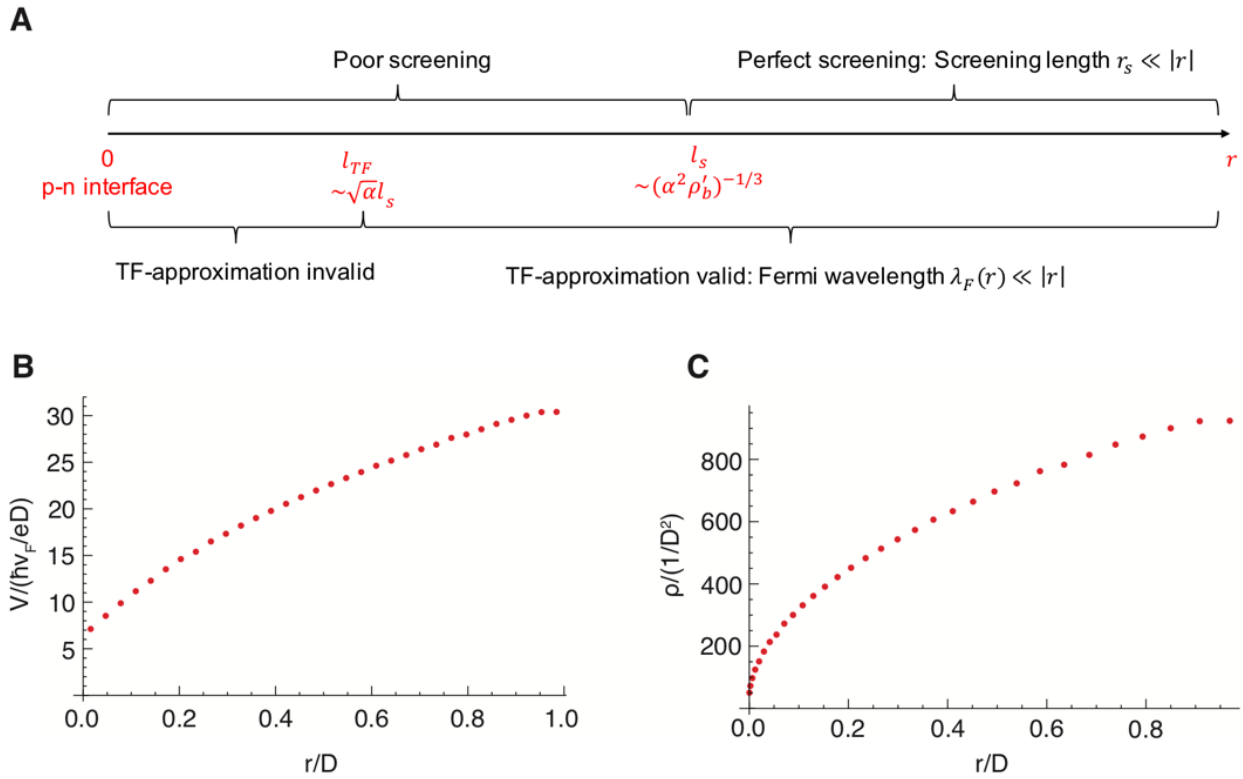

Fig. S6. Self-consistent screening near a p-n junction boundary. (A) Regions of perfect screening and Thomas Fermi approximation. $\alpha = e^2/(\kappa \hbar v_F)$ is the interaction constant, κ is the dielectric constant. ρ'_b is the density gradient at the p-n interface. **(B)** Electrostatic potential in units of $\sqrt{\pi}\hbar v_F / eD$. **(C)** Charge density in units of $1/D^2$.

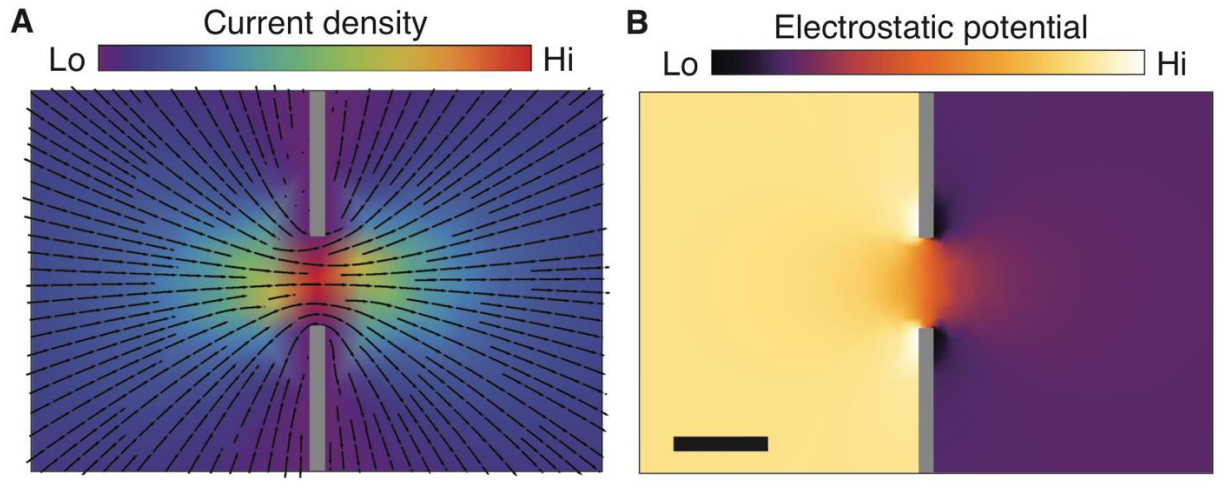

Fig. S7. Viscous fluid simulation of current flow through a 250 nm-wide slit. (A) Local current density. **(B)** Electrostatic potential. The scale bar is 250 nm.

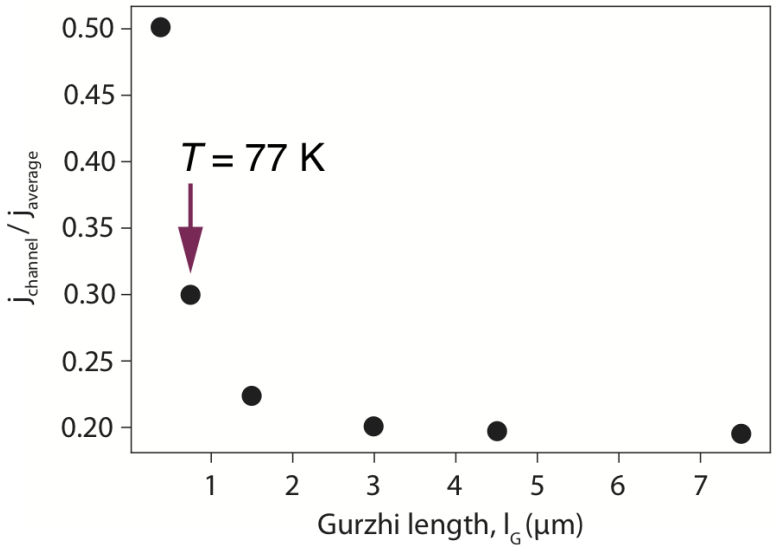

Fig. S8. Channel current density $j_{channel}$ as a function of Gurzhi length, normalized to the average current density across the entire width of the graphene flake, $j_{average}$.

References and Notes

1. M. Knudsen, The law of molecular flow and viscosity of gases moving through tubes. *Ann. Phys.* **28**, 75–130 (1909). doi:10.1002/andp.19093330106

2. Y. V. Sharvin, A possible method for studying Fermi surfaces. *Sov. Phys. JETP* **21**, 655–656 (1965).

3. R. Gurzhi, Minimum of resistance in impurity-free conductors. *Sov. Phys. JETP* **17**, 521–522 (1963).

4. R. Gurzhi, Hydrodynamic effects in solids at low temperature. *Sov. Phys. Usp.* **11**, 255–270 (1968). doi:10.1070/PU1968v011n02ABEH003815

5. L. W. Molenkamp, M. J. M. de Jong, Electron-electron-scattering-induced size effects in a two-dimensional wire. *Phys. Rev. B* **49**, 5038–5041 (1994). doi:10.1103/PhysRevB.49.5038 Medline

6. M. J. M. de Jong, L. W. Molenkamp, Hydrodynamic electron flow in high-mobility wires. *Phys. Rev. B* **51**, 13389–13402 (1995). doi:10.1103/PhysRevB.51.13389 Medline

7. X. P. A. Gao, G. S. Boebinger, A. P. Mills Jr., A. P. Ramirez, L. N. Pfeiffer, K. W. West, Strongly enhanced hole-phonon coupling in the metallic state of the dilute two-dimensional hole gas. *Phys. Rev. Lett.* **94**, 086402 (2005). doi:10.1103/PhysRevLett.94.086402 Medline

8. B. A. Braem, F. M. D. Pellegrino, A. Principi, M. Röösli, C. Gold, S. Hennel, J. V. Koski, M. Berl, W. Dietsche, W. Wegscheider, M. Polini, T. Ihn, K. Ensslin, Scanning gate microscopy in a viscous electron fluid. *Phys. Rev. B* **98**, 241304 (2018). doi:10.1103/PhysRevB.98.241304

9. A. D. Levin, G. M. Gusev, E. V. Levinson, Z. D. Kvon, A. K. Bakarov, Vorticity-induced negative nonlocal resistance in a viscous two-dimensional electron system. *Phys. Rev. B* **97**, 245308 (2018). doi:10.1103/PhysRevB.97.245308

10. G. M. Gusev, A. S. Jaroshevich, A. D. Levin, Z. D. Kvon, A. K. Bakarov, Stokes flow around an obstacle in viscous two-dimensional electron liquid. *Sci. Rep.* **10**, 7860 (2020). doi:10.1038/s41598-020-64807-6 Medline

11. A. Gupta, J. J. Heremans, G. Kataria, M. Chandra, S. Fallahi, G. C. Gardner, M. J. Manfra, Hydrodynamic and ballistic transport over large length scales in GaAs/AlGaAs. *Phys. Rev. Lett.* **126**, 076803 (2021). doi:10.1103/PhysRevLett.126.076803 Medline

12. M. Müller, J. Schmalian, L. Fritz, Graphene: A nearly perfect fluid. *Phys. Rev. Lett.* **103**, 025301 (2009). doi:10.1103/PhysRevLett.103.025301 Medline

13. I. Torre, A. Tomadin, A. K. Geim, M. Polini, Nonlocal transport and the hydrodynamic shear viscosity in graphene. *Phys. Rev. B* **92**, 165433 (2015). doi:10.1103/PhysRevB.92.165433

14. A. Principi, G. Vignale, M. Carrega, M. Polini, Bulk and shear viscosities of the two-dimensional electron liquid in a doped graphene sheet. *Phys. Rev. B* **93**, 125410 (2016). doi:10.1103/PhysRevB.93.125410

15. F. M. D. Pellegrino, I. Torre, A. K. Geim, M. Polini, Electron hydrodynamics dilemma: Whirlpools or no whirlpools. *Phys. Rev. B* **94**, 155414 (2016). doi:10.1103/PhysRevB.94.155414

16. L. Levitov, G. Falkovich, Electron viscosity, current vortices and negative nonlocal resistance in graphene. *Nat. Phys.* **12**, 672–676 (2016). doi:10.1038/nphys3667

17. H. Guo, E. Ilseven, G. Falkovich, L. S. Levitov, Higher-than-ballistic conduction of viscous electron flows. *Proc. Natl. Acad. Sci. U.S.A.* **114**, 3068–3073 (2017). doi:10.1073/pnas.1612181114 Medline

18. A. Stern, T. Scaffidi, O. Reuven, C. Kumar, J. Birkbeck, S. Ilani, How electron hydrodynamics can eliminate the Landauer-Sharvin resistance. *Phys. Rev. Lett.* **129**, 157701 (2022). doi:10.1103/PhysRevLett.129.157701 Medline

19. B. N. Narozhny, I. V. Gornyi, A. D. Mirlin, J. Schmalian, Hydrodynamic approach to electronic transport in graphene. *Ann. Phys.* **529**, 1700043 (2017). doi:10.1002/andp.201700043

20. A. Lucas, K. C. Fong, Hydrodynamics of electrons in graphene. *J. Phys. Condens. Matter* **30**, 053001 (2018). doi:10.1088/1361-648X/aaa274 Medline

21. D. Y. H. Ho, I. Yudhistira, N. Chakraborty, S. Adam, Theoretical determination of hydrodynamic window in monolayer and bilayer graphene from scattering rates. *Phys. Rev. B* **97**, 121404 (2018). doi:10.1103/PhysRevB.97.121404

22. G. Falkovich, L. Levitov, Linking spatial distributions of potential and current in viscous electronics. *Phys. Rev. Lett.* **119**, 066601 (2017). doi:10.1103/PhysRevLett.119.066601 Medline

23. A. Shytov, J. F. Kong, G. Falkovich, L. Levitov, Particle collisions and negative nonlocal response of ballistic electrons. *Phys. Rev. Lett.* **121**, 176805 (2018). doi:10.1103/PhysRevLett.121.176805 Medline

24. S. Danz, M. Titov, B. N. Narozhny, Giant nonlocality in nearly compensated two-dimensional semimetals. *Phys. Rev. B* **102**, 081114 (2020). doi:10.1103/PhysRevB.102.081114

25. M. S. Foster, I. L. Aleiner, Slow imbalance relaxation and thermoelectric transport in graphene. *Phys. Rev. B* **79**, 085415 (2009). doi:10.1103/PhysRevB.79.085415

26. A. Lucas, J. Crossno, K. C. Fong, P. Kim, S. Sachdev, Transport in inhomogeneous quantum critical fluids and in the Dirac fluid in graphene. *Phys. Rev. B* **93**, 075426 (2016). doi:10.1103/PhysRevB.93.075426

27. M. Zarenia, A. Principi, G. Vignale, Disorder-enabled hydrodynamics of charge and heat transport in monolayer graphene. *2D Mater.* **6**, 035024 (2019). doi:10.1088/2053-1583/ab1ad9

28. S. Li, A. Levchenko, A. V. Andreev, Hydrodynamic electron transport near charge neutrality. *Phys. Rev. B* **102**, 075305 (2020). doi:10.1103/PhysRevB.102.075305

29. A. Levchenko, J. Schmalian, Transport properties of strongly coupled electron-phonon liquids. *Ann. Phys.* **419**, 168218 (2020). doi:10.1016/j.aop.2020.168218

30. J. Gooth, F. Menges, N. Kumar, V. Süβ, C. Shekhar, Y. Sun, U. Drechsler, R. Zierold, C. Felser, B. Gotsmann, Thermal and electrical signatures of a hydrodynamic electron fluid in tungsten diphosphide. *Nat. Commun.* **9**, 4093 (2018). doi:10.1038/s41467-018-06688-y Medline

31. U. Vool, A. Hamo, G. Varnavides, Y. Wang, T. X. Zhou, N. Kumar, Y. Dovzhenko, Z. Qiu, C. A. C. Garcia, A. T. Pierce, J. Gooth, P. Anikeeva, C. Felser, P. Narang, A. Yacoby, Imaging phonon-mediated hydrodynamic flow in WTe_2. *Nat. Phys.* **17**, 1216–1220 (2021). doi:10.1038/s41567-021-01341-w

32. R. Krishna Kumar, D. Bandurin, F. M. D. Pellegrino, Y. Cao, A. Principi, H. Guo, G. H. Auton, M. Ben-Shalom, L. A. Ponomarenko, G. Falkovich, K. Watanabe, T. Taniguchi, I. V. Grigorieva, L. S. Levitov, M. Polini, A. K. Geim, Superballistic flow of viscous electron fluid through graphene constrictions. *Nat. Phys.* **13**, 1182–1185 (2017). doi:10.1038/nphys4240

33. D. A. Bandurin, I. Torre, R. Krishna Kumar, M. Ben Shalom, A. Tomadin, A. Principi, G. H. Auton, E. Khestanova, K. S. Novoselov, I. V. Grigorieva, L. A. Ponomarenko, A. K. Geim, M. Polini, Negative local resistance caused by viscous electron backflow in graphene. *Science* **351**, 1055–1058 (2016). doi:10.1126/science.aad0201 Medline

34. D. A. Bandurin, A. V. Shytov, L. S. Levitov, R. Krishna Kumar, A. I. Berdyugin, M. Ben Shalom, I. V. Grigorieva, A. K. Geim, G. Falkovich, Fluidity onset in graphene. *Nat. Commun.* **9**, 4533 (2018). doi:10.1038/s41467-018-07004-4 Medline

35. J. Crossno, J. K. Shi, K. Wang, X. Liu, A. Harzheim, A. Lucas, S. Sachdev, P. Kim, T. Taniguchi, K. Watanabe, T. A. Ohki, K. C. Fong, Observation of the Dirac fluid and the breakdown of the Wiedemann-Franz law in graphene. *Science* **351**, 1058–1061 (2016). doi:10.1126/science.aad0343 Medline

36. F. Ghahari, H.-Y. Xie, T. Taniguchi, K. Watanabe, M. S. Foster, P. Kim, Enhanced thermoelectric power in graphene: Violation of the Mott relation by inelastic scattering. *Phys. Rev. Lett.* **116**, 136802 (2016). doi:10.1103/PhysRevLett.116.136802 Medline

37. J. A. Sulpizio, L. Ella, A. Rozen, J. Birkbeck, D. J. Perello, D. Dutta, M. Ben-Shalom, T. Taniguchi, K. Watanabe, T. Holder, R. Queiroz, A. Principi, A. Stern, T. Scaffidi, A. K. Geim, S. Ilani, Visualizing Poiseuille flow of hydrodynamic electrons. *Nature* **576**, 75–79 (2019). doi:10.1038/s41586-019-1788-9 Medline

38. L. Ella, A. Rozen, J. Birkbeck, M. Ben-Shalom, D. Perello, J. Zultak, T. Taniguchi, K. Watanabe, A. K. Geim, S. Ilani, J. A. Sulpizio, Simultaneous voltage and current density imaging of flowing electrons in two dimensions. *Nat. Nanotechnol.* **14**, 480–487 (2019). doi:10.1038/s41565-019-0398-x Medline

39. A. Jenkins, S. Baumann, H. Zhou, S. A. Meynell, D. Yang, K. Watanabe, T. Taniguchi, A. Lucas, A. F. Young, A. C. Bleszynski Jayich, Imaging the breakdown of ohmic transport in graphene. *Phys. Rev. Lett.* **129**, 087701 (2022). doi:10.1103/PhysRevLett.129.087701 Medline

40. M. J. H. Ku, T. X. Zhou, Q. Li, Y. J. Shin, J. K. Shi, C. Burch, L. E. Anderson, A. T. Pierce, Y. Xie, A. Hamo, U. Vool, H. Zhang, F. Casola, T. Taniguchi, K. Watanabe, M. M.

Fogler, P. Kim, A. Yacoby, R. L. Walsworth, Imaging viscous flow of the Dirac fluid in graphene. *Nature* **583**, 537–541 (2020). doi:10.1038/s41586-020-2507-2 Medline

41. C. Kumar, J. Birkbeck, J. A. Sulpizio, D. Perello, T. Taniguchi, K. Watanabe, O. Reuven, T. Scaffidi, A. Stern, A. K. Geim, S. Ilani, Imaging hydrodynamic electrons flowing without Landauer-Sharvin resistance. *Nature* **609**, 276–281 (2022). doi:10.1038/s41586-022-05002-7 Medline

42. A. Aharon-Steinberg, T. Völkl, A. Kaplan, A. K. Pariari, I. Roy, T. Holder, Y. Wolf, A. Y. Meltzer, Y. Myasoedov, M. E. Huber, B. Yan, G. Falkovich, L. S. Levitov, M. Hücker, E. Zeldov, Direct observation of vortices in an electron fluid. *Nature* **607**, 74–80 (2022). doi:10.1038/s41586-022-04794-y Medline

43. S. Samaddar, J. Strasdas, K. Janßen, S. Just, T. Johnsen, Z. Wang, B. Uzlu, S. Li, D. Neumaier, M. Liebmann, M. Morgenstern, Evidence for local spots of viscous electron flow in graphene at moderate mobility. *Nano Lett.* **21**, 9365–9373 (2021). doi:10.1021/acs.nanolett.1c01145 Medline

44. J. Velasco Jr., L. Ju, D. Wong, S. Kahn, J. Lee, H.-Z. Tsai, C. Germany, S. Wickenburg, J. Lu, T. Taniguchi, K. Watanabe, A. Zettl, F. Wang, M. F. Crommie, Nanoscale control of rewriteable doping patterns in pristine graphene/boron nitride heterostructures. *Nano Lett.* **16**, 1620–1625 (2016). doi:10.1021/acs.nanolett.5b04441 Medline

45. E. I. Kiselev, J. Schmalian, Boundary conditions of viscous electron flow. *Phys. Rev. B* **99**, 035430 (2019). doi:10.1103/PhysRevB.99.035430

46. R. Moessner, N. Morales-Durán, P. Surówka, P. Witkowski, Boundary condition and geometry engineering in electronic hydrodynamics. *Phys. Rev. B* **100**, 155115 (2019). doi:10.1103/PhysRevB.100.155115

47. P. Muralt, D. W. Pohl, "Scanning tunneling potentiometry" in *Scanning Tunneling Microscopy* (Springer, 1986), pp. 252–254.

48. P. Muralt, H. Meier, D. W. Pohl, H. W. M. Salemink, Scanning tunneling microscopy and potentiometry on a semiconductor heterojunction. *Appl. Phys. Lett.* **50**, 1352–1354 (1987). doi:10.1063/1.97853

49. C. S. Chu, R. S. Sorbello, Scanning tunneling microscope as a probe of the local transport field in mesoscopic systems. *Phys. Rev. B* **40**, 5950–5955 (1989). doi:10.1103/PhysRevB.40.5950 Medline

50. T. Druga, M. Wenderoth, J. Homoth, M. A. Schneider, R. G. Ulbrich, A versatile high resolution scanning tunneling potentiometry implementation. *Rev. Sci. Instrum.* **81**, 083704 (2010). doi:10.1063/1.3469809 Medline

51. J. R. Kirtley, S. Washburn, M. J. Brady, Direct measurement of potential steps at grain boundaries in the presence of current flow. *Phys. Rev. Lett.* **60**, 1546–1549 (1988). doi:10.1103/PhysRevLett.60.1546 Medline

52. K. H. Bevan, A first principles scanning tunneling potentiometry study of an opaque graphene grain boundary in the ballistic transport regime. *Nanotechnology* **25**, 415701 (2014). doi:10.1088/0957-4484/25/41/415701 Medline

53. D. K. Morr, Scanning tunneling potentiometry, charge transport, and Landauer's resistivity dipole from the quantum to the classical transport regime. *Phys. Rev. B* **95**, 195162 (2017). doi:10.1103/PhysRevB.95.195162

54. B. G. Briner, R. M. Feenstra, T. P. Chin, J. M. Woodall, Local transport properties of thin bismuth films studied by scanning tunneling potentiometry. *Phys. Rev. B* **54**, R5283–R5286 (1996). doi:10.1103/PhysRevB.54.R5283 Medline

55. R. Landauer, Spatial variation of currents and fields due to localized scatterers in metallic conduction. *IBM J. Res. Develop.* **1**, 223–231 (1957). doi:10.1147/rd.13.0223

56. S.-H. Ji, J. B. Hannon, R. M. Tromp, V. Perebeinos, J. Tersoff, F. M. Ross, Atomic-scale transport in epitaxial graphene. *Nat. Mater.* **11**, 114–119 (2012). doi:10.1038/nmat3170 Medline

57. F. Giannazzo, I. Deretzis, A. La Magna, F. Roccaforte, R. Yakimova, Electronic transport at monolayer-bilayer junctions in epitaxial graphene on SiC. *Phys. Rev. B* **86**, 235422 (2012). doi:10.1103/PhysRevB.86.235422

58. W. Wang, K. Munakata, M. Rozler, M. R. Beasley, Local transport measurements at mesoscopic length scales using scanning tunneling potentiometry. *Phys. Rev. Lett.* **110**, 236802 (2013). doi:10.1103/PhysRevLett.110.236802 Medline

59. P. Willke, T. Druga, R. G. Ulbrich, M. A. Schneider, M. Wenderoth, Spatial extent of a Landauer residual-resistivity dipole in graphene quantified by scanning tunnelling potentiometry. *Nat. Commun.* **6**, 6399 (2015). doi:10.1038/ncomms7399 Medline

60. K. W. Clark, X.-G. Zhang, I. V. Vlassiouk, G. He, R. M. Feenstra, A. P. Li, Spatially resolved mapping of electrical conductivity across individual domain (grain) boundaries in graphene. *ACS Nano* **7**, 7956–7966 (2013). doi:10.1021/nn403056k Medline

61. A. Sinterhauf, G. A. Traeger, D. Momeni Pakdehi, P. Schädlich, P. Willke, F. Speck, T. Seyller, C. Tegenkamp, K. Pierz, H. W. Schumacher, M. Wenderoth, Substrate induced nanoscale resistance variation in epitaxial graphene. *Nat. Commun.* **11**, 555 (2020). doi:10.1038/s41467-019-14192-0 Medline

62. A. De Cecco, V. S. Prudkovskiy, D. Wander, R. Ganguly, C. Berger, W. A. de Heer, H. Courtois, C. B. Winkelmann, Non-invasive nanoscale potentiometry and ballistic transport in epigraphene nanoribbons. *Nano Lett.* **20**, 3786–3790 (2020). doi:10.1021/acs.nanolett.0c00838 Medline

63. J. P. Pelz, R. H. Koch, Tip-related artifacts in scanning tunneling potentiometry. *Phys. Rev. B* **41**, 1212–1215 (1990). doi:10.1103/PhysRevB.41.1212 Medline

64. J. Lee, D. Wong, J. Velasco Jr., J. F. Rodriguez-Nieva, S. Kahn, H.-Z. Tsai, T. Taniguchi, K. Watanabe, A. Zettl, F. Wang, L. S. Levitov, M. F. Crommie, Imaging electrostatically confined Dirac fermions in graphene quantum dots. *Nat. Phys.* **12**, 1032–1036 (2016). doi:10.1038/nphys3805

65. J. Velasco Jr., J. Lee, D. Wong, S. Kahn, H.-Z. Tsai, J. Costello, T. Umeda, T. Taniguchi, K. Watanabe, A. Zettl, F. Wang, M. F. Crommie, Visualization and control of single-electron charging in bilayer graphene quantum dots. *Nano Lett.* **18**, 5104–5110 (2018). doi:10.1021/acs.nanolett.8b01972 Medline

66. B. Brun, M. Moreau, S. Somanchi, V.-H. Nguyen, K. Watanabe, T. Taniguchi, J.-C. Charlier, C. Stampfer, B. Hackens, Imaging Dirac fermions flow through a circular Veselago lens. *Phys. Rev. B* **100**, 041401 (2019). doi:10.1103/PhysRevB.100.041401

67. See supplementary materials.

68. R. S. Sorbello, Residual-resistivity dipole in electron transport and electromigration. *Phys. Rev. B* **23**, 5119–5127 (1981). doi:10.1103/PhysRevB.23.5119

69. R. S. Sorbello, C. S. Chu, Residual resistivity dipoles, electromigration, and electronic conduction in metallic microstructures. *IBM J. Res. Develop.* **32**, 58–62 (1988). doi:10.1147/rd.321.0058

70. H. Guo, E. Ilseven, G. Falkovich, L. Levitov, Stokes paradox, back reflections and interaction-enhanced conduction. arXiv:1612.09239 [cond-mat.mes-hall] (2017).

71. C. Gutiérrez, D. Walkup, F. Ghahari, C. Lewandowski, J. F. Rodriguez-Nieva, K. Watanabe, T. Taniguchi, L. S. Levitov, N. B. Zhitenev, J. A. Stroscio, Interaction-driven quantum Hall wedding cake-like structures in graphene quantum dots. *Science* **361**, 789–794 (2018). doi:10.1126/science.aar2014 Medline

72. E. A. Quezada-López, Z. Ge, T. Taniguchi, K. Watanabe, F. Joucken, J. Velasco Jr., Comprehensive electrostatic modeling of exposed quantum dots in graphene/hexagonal boron nitride heterostructures. *Nanomaterials* **10**, 1154 (2020). doi:10.3390/nano10061154 Medline

73. W. A. Behn, Z. J. Krebs, K. J. Smith, K. Watanabe, T. Taniguchi, V. W. Brar, Measuring and tuning the potential landscape of electrostatically defined quantum dots in graphene. *Nano Lett.* **21**, 5013–5020 (2021). doi:10.1021/acs.nanolett.1c00791 Medline

74. J. A. Støvneng, P. Lipavský, Thermopower in scanning-tunneling-microscope experiments. *Phys. Rev. B* **42**, 9214–9216 (1990). doi:10.1103/PhysRevB.42.9214 Medline

75. J. Park, G. He, R. M. Feenstra, A.-P. Li, Atomic-scale mapping of thermoelectric power on graphene: Role of defects and boundaries. *Nano Lett.* **13**, 3269–3273 (2013). doi:10.1021/nl401473j Medline

76. A. Lucas, Stokes paradox in electronic Fermi liquids. *Phys. Rev. B* **95**, 115425 (2017). doi:10.1103/PhysRevB.95.115425

77. S. S. Pershoguba, A. F. Young, L. I. Glazman, Current distribution in a slit connecting two graphene half planes. *Phys. Rev. B* **102**, 125404 (2020). doi:10.1103/PhysRevB.102.125404

78. S. Li, M. Khodas, A. Levchenko, Conformal maps of viscous electron flow in the Gurzhi crossover. *Phys. Rev. B* **104**, 155305 (2021). doi:10.1103/PhysRevB.104.155305

79. J. Geurs, Y. Kim, K. Watanabe, T. Taniguchi, P. Moon, J. H. Smet, Rectification by hydrodynamic flow in an encapsulated graphene Tesla valve. arXiv:2008.04862 [cond-mat.mes-hall] (2020).

80. Z. J. Krebs, W. A. Behn, S. Li, K. J. Smith, K. Watanabe, T. Taniguchi, A. Levchenko, V. W. Brar, Imaging the breaking of electrostatic dams in graphene for ballistic and viscous fluids, version 1, Zenodo (2022); https://doi.org/10.5281/zenodo.7314592.

81. L. Wang, I. Meric, P. Y. Huang, Q. Gao, Y. Gao, H. Tran, T. Taniguchi, K. Watanabe, L. M. Campos, D. A. Muller, J. Guo, P. Kim, J. Hone, K. L. Shepard, C. R. Dean, One-dimensional electrical contact to a two-dimensional material. *Science* **342**, 614–617 (2013). doi:10.1126/science.1244358 Medline

82. C. R. Dean, A. F. Young, I. Meric, C. Lee, L. Wang, S. Sorgenfrei, K. Watanabe, T. Taniguchi, P. Kim, K. L. Shepard, J. Hone, Boron nitride substrates for high-quality graphene electronics. *Nat. Nanotechnol.* **5**, 722–726 (2010). doi:10.1038/nnano.2010.172 Medline

83. S. Das Sarma, S. Adam, E. H. Hwang, E. Rossi, Electronic transport in two-dimensional graphene. *Rev. Mod. Phys.* **83**, 407–470 (2011). doi:10.1103/RevModPhys.83.407

84. L. M. Zhang, M. M. Fogler, Nonlinear screening and ballistic transport in a graphene p-n junction. *Phys. Rev. Lett.* **100**, 116804 (2008). doi:10.1103/PhysRevLett.100.116804 Medline